RSC Advances

PAPER

View Article Online
View Journal | View Issue

Cite this: *RSC Adv.*, 2026, **16**, 15430

$BaO_2/Mn_2O_3/ZnO/BaMnO_3$ nanocomposite: structural, optical, spectral, morphological and antibacterial properties

Adnan Alnehia, *[a] Mohamed E. El Sayed,[b] Mohammad N. Murshed,[cd] Abduelwhab B. Alwany[de] and Ahmed Samir[b]

This work presents the inaugural synthesis and detailed characterization of a novel $BaO_2/Mn_2O_3/ZnO/BaMnO_3$ nanocomposite fabricated *via* a straightforward co-precipitation technique, utilizing solely distilled water as the solvent, followed by calcination at 500 °C for two hours. This eco-friendly approach marks a notable improvement over conventional methods by eliminating the use of harmful organic solvents. Comprehensive analyses, including XRD, SEM, EDX, TEM, TGA, and UV-Vis spectroscopy were employed to elucidate the structural, morphological, optical, and thermal features of the synthesized material. XRD results confirmed the successful formation of the composite phase with an average crystallite size below 85 nm. EDX spectra verified the presence of constituent elements (Ba, Mn, Zn, O) with no detectable contaminants. Fourier-transform infrared (FTIR) measurements further supported the synthesis of the corresponding oxide phases. Optical investigations indicated a band gap value of approximately 2.74 eV. Thermal analysis demonstrated remarkable stability, signifying suitability for applications involving elevated temperatures. Antibacterial efficacy was assessed against Gram-negative *E. coli* and Gram-positive *S. aureus* through the disc diffusion assay. The nanocomposite displayed pronounced antibacterial activity, yielding a zone of inhibition measuring 13 mm against *S. aureus*. These findings underscore the potential of the material in thermal sterilization applications and as antimicrobial coatings within healthcare and industrial settings. Future work will delve into the antibacterial mechanism and expand application-oriented studies.

Received 25th January 2026
Accepted 9th March 2026

DOI: 10.1039/d6ra00680a

rsc.li/rsc-advances

1 Introduction

Nanomaterials, with their exceptionally small dimensions (typically 1–100 nm), exhibit unique physicochemical properties distinct from their bulk counterparts.[1–3] These properties, arising from high surface-to-volume ratios, quantum confinement effects, and altered electronic structures, have positioned nanocomposites at the forefront of materials science research.[1,2] Their versatility has led to an explosion of interest across diverse fields, including electronics, catalysis, energy storage, sensing, and biomedical applications, offering solutions to various technological and environmental challenges.[4] Among the vast array of nanomaterials, multi-component metal oxide nanocomposites have garnered significant attention due to their synergistic effects, where the combination of different metal oxides often leads to enhanced or novel properties not observed in individual components.[5–9] Barium oxide (BaO_2), manganese oxides (*e.g.*, Mn_2O_3), zinc oxide (ZnO), and barium manganate ($BaMnO_3$) are individually recognized for their distinct characteristics.[10] BaO_2 is known for its oxidative properties,[11,12] Mn_2O_3 for its catalytic and magnetic applications,[13–16] and ZnO for its wide bandgap semiconducting properties, making it valuable in optoelectronics and antimicrobial applications.[17–19] $BaMnO_3$, a perovskite-type manganate, has shown promise in catalysis, magnetic, and dielectric applications.[10,20] The deliberate combination of these distinct metal oxides into a single nanocomposite structure offers an exciting avenue to create a material with a multifaceted functionality that leverages the best attributes of each constituent. Despite the promising potential of such multi-component systems, the specific combination of BaO_2, Mn_2O_3, ZnO, and $BaMnO_3$ into a single nanocomposite ($BaO_2/Mn_2O_3/ZnO/BaMnO_3$) has, to the best of our knowledge, remained largely unexplored in the scientific literature. Existing synthesis routes for complex metal oxide nanocomposites often involve sophisticated equipment or the use of various organic solvents, which can be costly, time-consuming, and environmentally hazardous. This research gap highlights an opportunity to not only synthesize this novel

[a]*Department of Physics, Faculty of Applied Sciences, Thamar University, 87246 Dhamar, Yemen. E-mail: adnanalnahia83@gmail.com*
[b]*Health Specialties, Basic Sciences and Applications Unit, Applied College, King Khalid University, Mohayil Asir Abha, 61421, Saudi Arabia*
[c]*Physics Department, Faculty of Science, King Khalid University, Abha, Saudi Arabia*
[d]*Physics Department, Faculty of Applied Science, Ibb University, 70270 Ibb, Yemen*
[e]*Faculty of Science and Engineering, Aljazeera University, Ibb, Yemen*

multi-component system but also to develop a more environmentally benign and scalable synthesis approach.

Therefore, this study aims to report the facile, first-time synthesis of the $BaO_2/Mn_2O_3/ZnO/BaMnO_3$ nanocomposite using a straightforward and eco-friendly co-precipitation method, utilizing only distilled water as the solvent. Following calcination, the resulting nanocomposite was subjected to comprehensive characterization to elucidate its structural, optical, spectral, and morphological properties using X-ray Diffraction (XRD), Scanning Electron Microscopy (SEM), Energy Dispersive X-ray spectroscopy (EDX), Transmission Electron Microscopy (TEM), UV-Visible spectroscopy, and Fourier-Transform Infrared (FTIR) spectroscopy. Furthermore, a critical aspect of this research involves evaluating the antibacterial efficacy of the synthesized $BaO_2/Mn_2O_3/ZnO/BaMnO_3$ nanocomposite against both Gram-positive and Gram-negative bacterial strains, thereby exploring its potential for applications in antimicrobial materials and beyond.

2 Experimental procedures

2.1 Materials

Manganese(II) chloride tetrahydrate ($MnCl_2 \cdot 4H_2O$, 99% purity, Fluka-Garantie), sodium hydroxide (NaOH), barium chloride ($BaCl_2 \cdot 2H_2O$, 99%, Himedia), and distilled water were utilized as received without any additional purification. Zinc nitrate hexahydrate ($Zn(NO_3)_2 \cdot 6H_2O$, BDH, 98%) was also employed in its original form.

2.2 Synthesis method

To synthesize the $BaO_2/Mn_2O_3/ZnO/BaMnO_3$ nanocomposite, the following experimental protocol was employed: initially, 2.44 g of barium chloride ($BaCl_2 \cdot 2H_2O$) was dissolved in 20 mL of distilled water to prepare a 0.5 M solution. This solution was stirred continuously at ambient temperature for 20 minutes to ensure complete dissolution. Similarly, a separate solution of manganese(II) chloride ($MnCl_2$) was prepared by dissolving 1.258 g in 20 mL of distilled water under identical conditions and stirring duration, also yielding a 0.5 M concentration. In parallel, zinc nitrate hexahydrate ($Zn(NO_3)_2 \cdot 6H_2O$), weighing 2.97 g, was dissolved in another 20 mL portion of distilled water and stirred for 20 minutes at room temperature. Subsequently, these three precursor solutions were combined into a single beaker and subjected to magnetic stirring at room temperature for two hours to achieve thorough mixing and homogeneity. Separately, 2.4 g of sodium hydroxide (NaOH) was dissolved in distilled water to prepare a 3 M solution, with continuous magnetic stirring for twenty minutes until completely dissolved. This alkaline solution was then added dropwise into the mixed metal precursor solution while maintaining vigorous stirring. The pH of the reaction mixture was carefully adjusted to approximately 10 during this addition. The resulting suspension underwent further stirring for an additional two hours employing the co-precipitation technique to facilitate nanocomposite formation. The precipitate formed was collected by filtration using filter paper and subsequently dried in an oven at 200 °C for two hours to remove residual moisture. After drying, the solid product was finely ground into powder form using a mortar and pestle to ensure uniform particle size distribution. Finally, the powdered sample was placed in a crucible and subjected to calcination at 500 °C for two hours to promote crystallinity and phase formation within the nanocomposite material.[21] The obtained fine powder of $BaO_2/Mn_2O_3/ZnO/BaMnO_3$ nanocomposite was stored in a clean container under dry conditions until further characterization measurements were performed. Fig. 1 provides a visual representation of the preparation process.

Reaction mechanism:

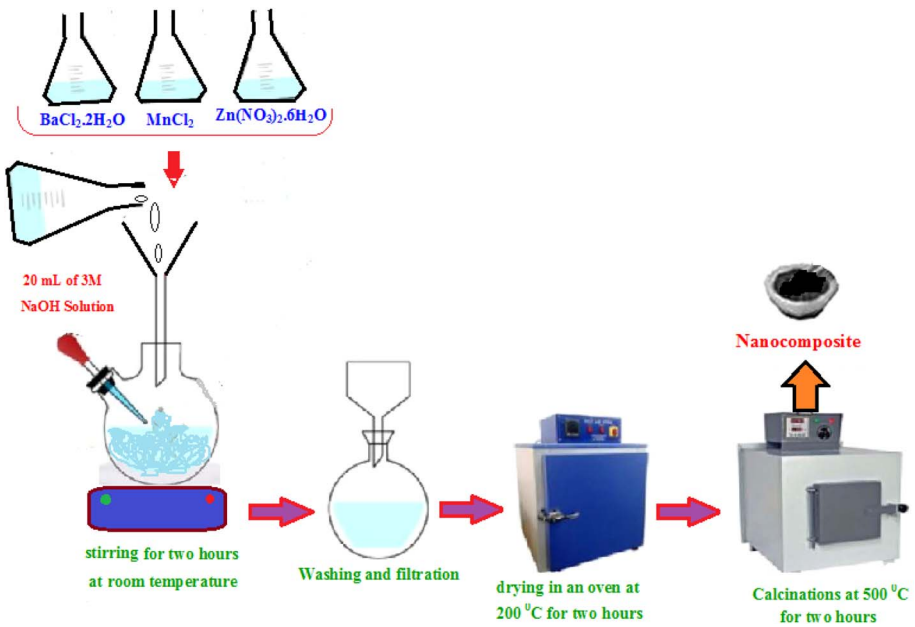

Fig. 1 Schematic presentation of nanocomposite.

During the experimentation, each stage in the manufacture of following nanocomposite can be observed as follows:

Step 1: dissolution of the metal salts in water individually:

$$BaCl_2 \cdot 2H_2O\ (solid) \rightarrow Ba^{2+}\ (aq) + 2Cl^-\ (aq) + 2H_2O$$

$$MnCl_2\ (solid) \rightarrow Mn^{2+}\ (aq) + 2Cl^-\ (aq)$$

$$Zn(NO_3)_2 \cdot 6H_2O\ (solid) \rightarrow Zn^{2+}\ (aq) + 2NO_3^-\ (aq) + 6H_2O$$

Step 2: mixing the three solutions to form a combined aqueous solution containing Ba^{2+}, Mn^{2+}, and Zn^{2+} ions.

Step 3: preparation of NaOH solution (3 M):

$$NaOH\ (solid) \rightarrow Na^+\ (aq) + OH^-\ (aq)$$

Step 4: adding NaOH solution dropwise to the mixed metal ions solution under continuous stirring to precipitate the corresponding metal hydroxides:

$$Ba^{2+}\ (aq) + 2OH^-\ (aq) \rightarrow Ba(OH)_2\ (s)$$

$$Mn^{2+}\ (aq) + 2OH^-\ (aq) \rightarrow Mn(OH)_2\ (s)$$

$$Zn^{2+}\ (aq) + 2OH^-\ (aq) \rightarrow Zn(OH)_2\ (s)$$

Step 5: after mixing and aging for 2 hours at room temperature, the precipitates are filtered and dried at 200 °C. Some initial dehydration and partial transformation may occur, such as:

$$Ba(OH)_2\ (s) \rightarrow BaO + H_2O\ (g)\ [partial\ dehydration]$$

$$Mn(OH)_2\ (s) \rightarrow MnO + H_2O\ (g)\ [partial\ dehydration]$$

$$Zn(OH)_2\ (s) \rightarrow ZnO + H_2O\ (g)\ [dehydration]$$

Step 6: calcination of the dried powder at 500 °C for 2 hours in air leads to oxidation and formation of mixed oxides:

$$4BaO + O_2 \rightarrow 2BaO_2\ (barium\ peroxide\ formation)$$

$$4MnO + O_2 \rightarrow 2Mn_2O_3\ (manganese\ oxide\ oxidation)$$

ZnO remains stable oxide as ZnO

$$BaO + Mn_2O_3 \rightarrow BaMnO_3\ (mixed\ barium\ manganate\ perovskite)$$

Overall, the key formed phases after calcination are BaO_2, Mn_2O_3, ZnO, and $BaMnO_3$.

2.3 Characterization techniques

The optical properties were assessed using a Hitachi U3900 UV-Vis spectrophotometer (Tokyo, Japan) equipped with Varian Cary-50 software, which allowed for the measurement of wavelengths ranging from 200 to 800 nm at ambient temperature. XRD analysis was executed utilizing a Shimadzu EDX-720 diffractometer (Kyoto, Japan) with CuK_α radiation ($\lambda = 1.5418$ Å), scanning the 2θ range from 15° to 75° at a scanning rate of 4° per minute. Thermal gravimetric analysis (TGA) was performed on a Mettler Toledo TGA/DSC1 star system (Columbus, OH, USA), where approximately 10 mg of each sample was heated from 25 °C to 1200 °C at a heating rate of 25 °C per minute under an air atmosphere. FTIR spectra were recorded using a Nicolet iS10 FTIR spectrometer (Thermo Scientific, Madison, WI, USA) equipped with a diamond ATR accessory, over 500–4000 cm^{-1}, at 4 cm^{-1} resolution, averaging 32 scans per spectrum. TEM images were captured using an FEI Tecnai F20 ST microscope (FEI Co., OR, USA) operating at an acceleration voltage of 200 kV. Additionally, SEM and EDX analyses were carried out using instrumentation supplied by Jeol Ltd (Tokyo, Japan).

3 Results and discussion

3.1 XRD analysis

The crystalline structure of the $BaO_2/Mn_2O_3/ZnO/BaMnO_3$ nanocomposite was meticulously investigated using XRD techniques to elucidate the phase composition and microstructural characteristics. The diffraction pattern exhibited sharp and distinct peaks at characteristic 2θ angles (see Fig. 2), systematically arranged according to the standard reference patterns from JCPDS (cards 07-0233, 41-1442, 36-1451, and 71-1521). These phase identifications confirmed the simultaneous presence of the tetragonal phase of BaO_2, the cubic phase of Mn_2O_3, the hexagonal phase of ZnO, and the hexagonal phase of $BaMnO_3$, indicating the successful synthesis of the targeted multi-phase nanocomposite.

The average crystallite sizes for each phase were estimated using the Debye–Scherrer equation, $D = 0.9\lambda/(\beta \cos\theta)$, where λ represents the X-ray wavelength (0.154 nm), β is the full width at

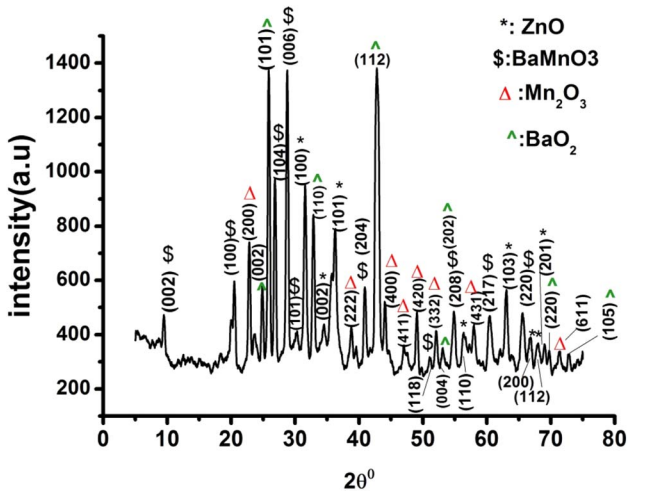

Fig. 2 XRD spectra of the $BaO_2/Mn_2O_3/ZnO/BaMnO_3$ nanocomposite.

Table 1 Crystallite size, micro-strain and SSA

Oxide	Crystallite size (nm)	Dislocation density (δ) $\times 10^{14}$ (1/m^2)	Lattice-strain	Lattice-strain from W–H analysis
BaO_2	83.01	1.451	0.000645	−0.00184
Mn_2O_3	44.95	4.951	0.000887	−0.00006
ZnO	47.37	4.457	0.000814	−0.00003
$BaMnO_3$	66.81	2.241	0.000603	0.000197

half maximum (FWHM), and θ is the Bragg angle.[22–25] The calculated crystallite dimensions ranged from approximately 40 nm to 84 nm across different phases. These nanoscale dimensions suggest effective control over the formation and growth mechanisms during synthesis, playing a pivotal role in influencing the physical and chemical properties of the nanocomposite.

In addition to size determination, precise parameters such as dislocation density (δ) and microstrain (ε) were derived to provide deeper insights into lattice defects and intrinsic stresses within the material. The δ was evaluated using $\delta = 1/D^2$, while microstrain was calculated through $\varepsilon = \beta \cos\theta/4$, offering valuable perspectives on the nature of defects in the nanocomposite structure.[26–28] Furthermore, Williamson–Hall analysis was employed for a more accurate assessment of lattice strain, utilizing the relation $\beta \cos\theta = (K\lambda/D) + 4\varepsilon \sin\theta$.[29] The results revealed significant intrinsic strain, likely attributed to lattice mismatches at the interfaces of different crystalline phases.[30] This self-induced lattice strain is crucial as it can enhance certain functional properties such as electrical conductivity and catalytic activity, while potentially detracting from mechanical durability and structural stability. Therefore, understanding and fine-tuning these effects through meticulous analysis is essential for optimizing material performance for specific applications,[21,28] as illustrated in Table 1.

Considering the nanoscale dimensions of the crystallites, the specific surface area (SSA) was calculated using the empirical formula SSA $= 6 \times 1000/(D \times \rho)$, where D is the crystallite size and ρ is the corresponding density. This parameter is vital for linking surface phenomena such as catalytic activity or adsorption capacity to structural characteristics.[31] Additionally, crystallinity was quantitatively assessed by comparing the integrated areas under the crystal peaks (A_{cp}) to the total diffraction intensity (A_{ta}) using the formula: crystallinity (%) $= (A_{cp}/A_{ta}) \times 100\%$. This ratio serves to evaluate the purity and ordering of crystalline phases within the nanocomposite,[32] as detailed in Table 2.

Table 2 The SSA, space group and, crystallinity for $BaO_2/Mn_2O_3/ZnO/BaMnO_3$

Oxides	SSA(m^2 g^{-1})	Space group	Crystallinity (%)
BaO_2	12.823	$I4/mmm$	83.89
Mn_2O_3	26.966	$Ia\bar{3}$	
ZnO	22.319	$P6_3mc$	
$BaMnO_3$	14.665	$P6_3/mmc$	

In summary, the X-ray diffraction analysis results provide compelling evidence for the successful synthesis of a multiphase $BaO_2/Mn_2O_3/ZnO/BaMnO_3$ nanocomposite, offering a comprehensive understanding of its structural complexities at the nanoscale. Detailed analyses of crystallite size distribution, lattice strain effects, surface area considerations, and crystallinity underscore the critical role of XRD in establishing the relationship between structure and properties. These insights facilitate precise tuning of synthesis parameters to achieve optimal nanocomposite performance tailored to various technological applications.

3.2 FTIR analysis

FTIR spectroscopy was employed to examine the surface functionalities and metal–oxygen bonding environment of the $BaO_2/Mn_2O_3/ZnO/BaMnO_3$ nanocomposite (Fig. 3a), with an enlarged view of the fingerprint region shown in Fig. 2b. A broad absorption centered at about 3324 cm^{-1} is assigned to O–H stretching from surface hydroxyls and/or physisorbed water, which is typical for oxide nanopowders synthesized and handled under ambient conditions.[11,33] The band observed at 1661 cm^{-1} correspond predominantly to the H–O–H bendingvibration of adsorbed water, consistent with the presence of the broad O–H stretching envelope.[34] A strong band at 1424 cm^{-1}, together with the distinct feature at 880 cm^{-1}, is characteristic of carbonate (CO_3^{2-}) species, where the1420–

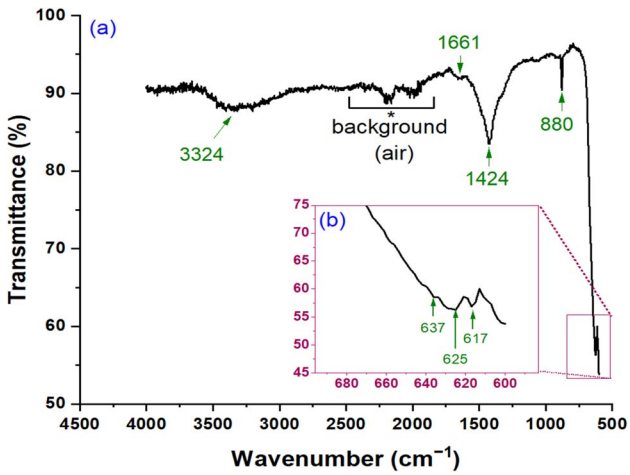

Fig. 3 FTIR spectra of $BaO_2/Mn_2O_3/ZnO/BaMnO_3$ nanocomposite.

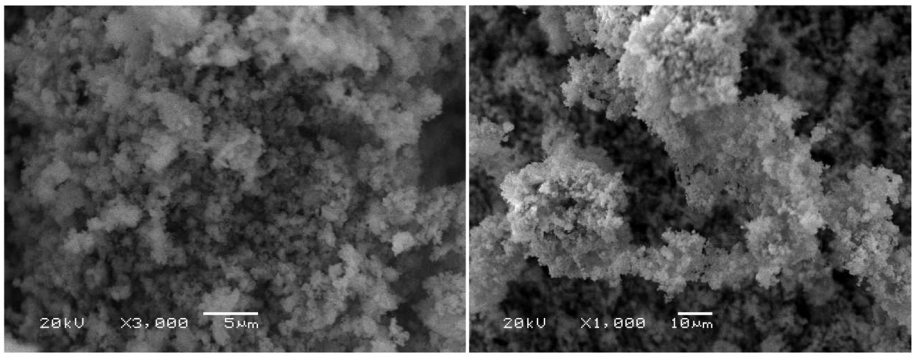

Fig. 4 SEM image of $BaO_2/Mn_2O_3/ZnO/BaMnO_3$ nanocomposite.

1460 cm^{-1} region is commonly attributed to the asymmetric stretching mode (ν_3) and the 880 cm^{-1} band to a carbonate bending mode (ν_3).[35] The presence of carbonate is chemically reasonable for Ba-containing oxide/peroxide systems, since BaO/BaO_2-based surfaces readily uptake atmospheric CO_2, producing surface $BaCO_3$-like species upon exposure to air; thus, these bands could reflect such situation of surface carbonation rather than the contaminationwith organic components.[35]

In the low-wavenumber region (Fig. 3b), the composite shows multiple absorptions at 637, 625, and 617 cm^{-1}. These features fall in the range expected for metal–oxygen lattice vibrations in mixed oxides; for example, Zn–O stretching is commonly reported within 400–600 cm^{-1} (often broadened/shifted by particle size, crystallinity, and composite formation), while perovskite-type manganite materials frequently exhibit a prominent band around 600 cm^{-1} associated with Mn–O/MnO_6 octahedral stretching and related Mn–O–Mn vibrations.[16,36–38] Because lattice modes of ZnO, Mn-oxides, and Ba–manganite phases overlap strongly in the 700–500 cm^{-1} region, FTIR is best interpreted as confirming the presence of M–O frameworks and surface functionalities, whereas phase identification and crystal symmetry assignments should be based primarily on XRD.[37]

3.3 SEM analysis

The surface morphology of the quaternary nanocomposite was meticulously examined using Scanning Electron Microscopy (SEM), as illustrated in Fig. 4. The SEM images, captured at two distinct magnifications, reveal a densely packed structure comprising nanoscale aggregates and smaller, less agglomerated nanoparticles. The nanoparticles exhibit a quasi-spherical morphology, albeit with irregular shapes and sizes, and a notably rough surface texture. Furthermore, Energy-

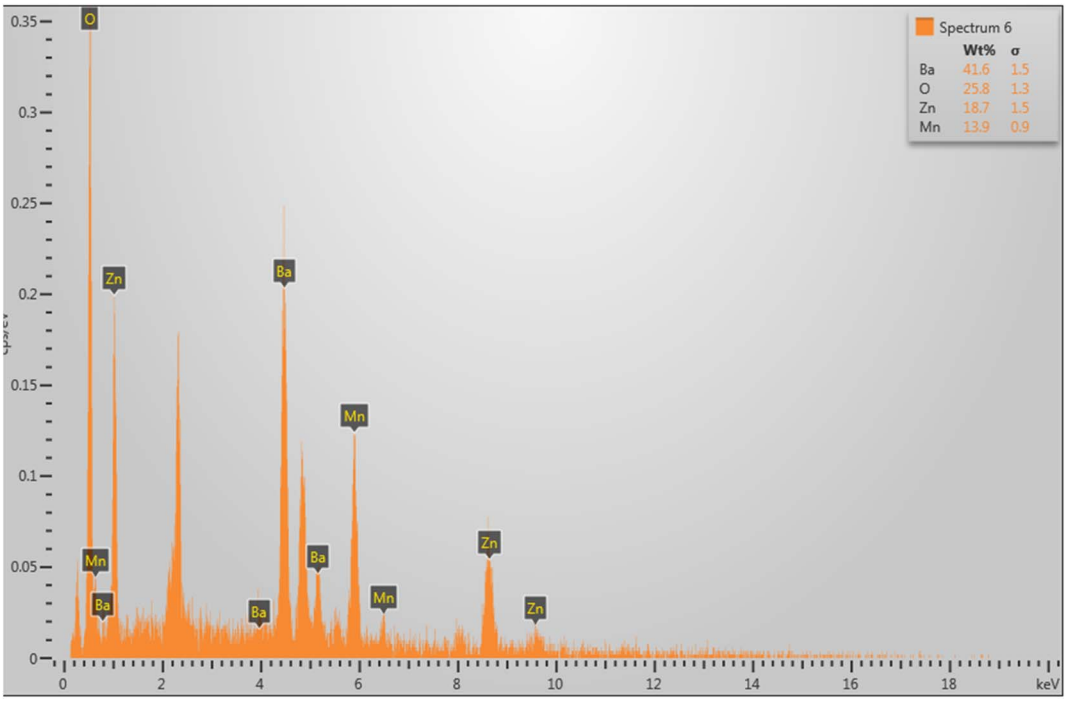

Fig. 5 EDX of $BaO_2/Mn_2O_3/ZnO/BaMnO_3$ nanocomposite.

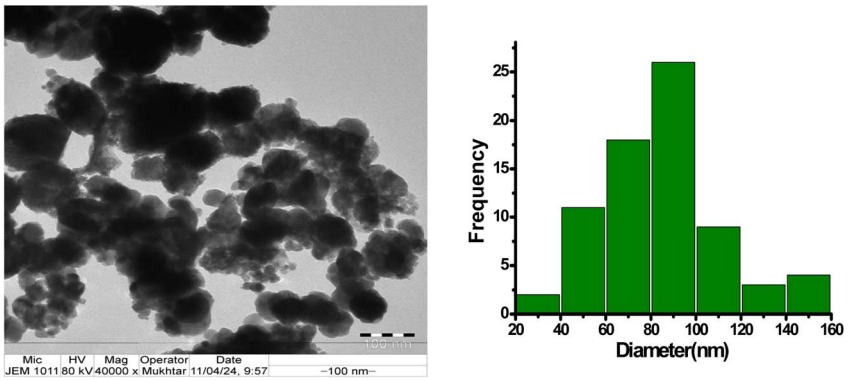

Fig. 6 TEM image and particle size distribution of $BaO_2/Mn_2O_3/ZnO/BaMnO_3$ nanocomposite.

Dispersive X-ray (EDX) spectroscopy was employed to determine the elemental composition of the nanocomposite, with the results presented in Fig. 5. The EDX analysis unequivocally confirms the presence of barium, manganese, zinc, and oxygen, which is consistent with the intended composition of the nanocomposite. Notably, no additional elements or impurities were detected, attesting to the high purity of the synthesized material.

The SEM and EDX analyses provide compelling insights into the morphology and composition of the quaternary nanocomposite. The densely packed structure and quasi-spherical nanoparticle morphology suggest potential applications in various fields, including catalysis, energy storage, and biomedical devices. The confirmation of the elemental composition and the absence of impurities demonstrate the successful synthesis of the nanocomposite material, which is essential for achieving the desired properties and performance. The rough surface texture and nanoscale aggregates may also contribute to the material's enhanced surface area and reactivity, making it an attractive candidate for various technological applications.

3.4 TEM analysis

TEM was employed to analyze the morphology and particle size distribution of the synthesized nanocomposite, as depicted in Fig. 6. The TEM micrographs reveal that the nanoparticles are predominantly quasi-spherical; however, a noticeable heterogeneity in both shape and size is evident. This morphological variation reflects the presence of multiple crystallographic phases within the composite, including hexagonal ZnO, cubic Mn_2O_3, tetragonal BaO_2, and hexagonal $BaMnO_3$. Such a multiphase system accounts for the observed diversity in particle dimensions. Quantitative analysis of the TEM images resulted in an average particle size of 89.77 nm, with a notable dispersion attributed to the complex, multi-phase nature of the material. This structural complexity is further confirmed by the broad particle size distribution histogram derived from the micrographs. The interplay between these diverse morphologies and crystalline structures is expected to significantly influence the physical and chemical behaviors of the nanocomposite. Overall, the TEM investigation validates the successful fabrication of a structurally intricate nanocomposite composed of quasi-spherical nanoparticles exhibiting varied sizes and shapes. These characteristics are anticipated to impart unique functional properties to the material, underscoring its potential suitability for a wide range of advanced applications. The present study thus provides crucial morphological insights that contribute to understanding the composite's structure–property relationships, strengthening the case for its significance and originality in the field.

3.5 TGA analysis

TGA and derivative thermogravimetry (DTG) were used to evaluate the thermal stability and volatile species of the $BaO_2/Mn_2O_3/ZnO/BaMnO_3$ nanocomposite,as shown in Fig. 7. The TG profile shows a gradual total mass loss of about 8–9 wt% up to 900 °C, confirming the predominantly inorganic nature and high thermal stability of the composite, as detailed in Table 3. The DTG curve resolves this loss into four regions. Stage I (RT–240 °C) exhibits a DTG minimum at 193 °C and is assigned to desorption of physically adsorbed moisture.[39] Stage II (240–502 °C) shows a DTG feature near 290 °C attributed mainly to removal of strongly bound water and dehydroxylation of surface

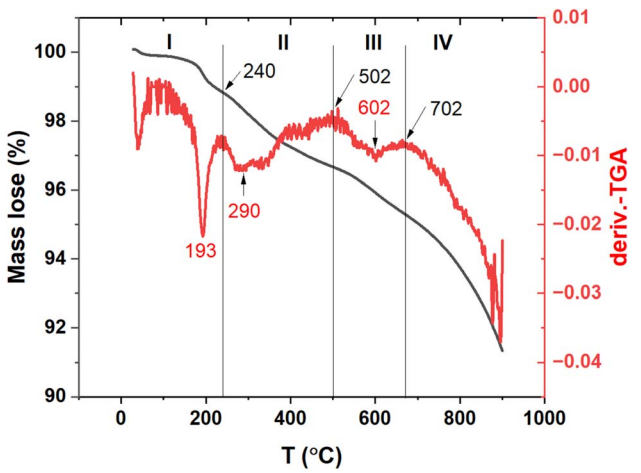

Fig. 7 TGA analysis of $BaO_2/Mn_2O_3/ZnO/BaMnO_3$ nanocomposite.

Table 3 Weight loss changes recorded from the TGA of precursor sample

Stage	Temperature range (°C)	DTG (°C)	Main process (most likely)	Typical evolved species	Mass change (est.)
I	RT–240	193	Desorption of physically adsorbed moisture and weakly bound water	H_2O	1.1 wt%
II	240–502	290	Dehydroxylation of surface –OH; loss of strongly bound water and residual hydroxylated species from wet synthesis	H_2O	2.2 wt%
III	502–702	602	Minor lattice relaxation, oxygen non-stoichiometry in Mn–O frameworks	O_2	1.5 wt%
IV	702–900	702 (shoulder)	Decarbonation of Ba-carbonate surface species; continued oxygen non-stoichiometry at high T	CO_2 (dominant), O_2 (possible)	3.5 wt%
Total	RT–900	—	—	—	8.5 wt%

–OH groups formed during wet synthesis. Stage III (502–702 °C) presents a DTG minimum at 602 °C, consistent with structural relaxation and mild oxygen non-stoichiometry changes of Mn–O frameworks and/or the onset of carbonate evolution.[16,40] Stage IV (702–900 °C) corresponds to the major high-temperature contribution, consistent with the decarbonation of the proposed Ba-carbonate surface species and continued oxygen non-stoichiometry at elevated temperature. These assignments are consistent with the FTIR evidence for surface hydroxylation, hydration and carbonate species.

3.6 UV-visible analysis

The optical properties of the $BaO_2/Mn_2O_3/ZnO/BaMnO_3$ nanocomposite were thoroughly investigated using UV-Visible (UV-Vis) spectroscopy, with the absorption spectrum recorded across the 200–900 nm wavelength range as depicted in Fig. 8. The spectrum reveals strong absorption in the ultraviolet region with a gradual decline toward longer wavelengths, consistent with the intrinsic electronic transitions of the constituent oxides. Unlike individual components, the nanocomposite absorption profile does not exhibit sharp and distinct absorption peaks; this broad spectral response stems from the synergistic interaction and overlapping electronic states of the multiple oxide phases collaboratively influencing the optical behavior. To quantify the optical band gap, the Tauc plot methodology [41,42] was employed (Fig. 9), yielding an estimated band gap energy of approximately 2.74 eV for the synthesized nanocomposite. This intermediate band gap value notably lies between those reported for the individual oxide components, which are approximately 4.38 eV for BaO_2,[43] 3.32 eV for ZnO,[44] and 1.8 eV for Mn_2O_3.[45] The reduction in band gap relative to the wide band gap BaO_2 and ZnO phases can be attributed to the incorporation of Mn_2O_3 and the formation of mixed oxide interfaces, which induce electronic coupling and create localized states within the band structure, effectively narrowing the overall band gap of the composite material. This tailored ban dgap within the visible region enables effective absorption of solar UV-Vis radiation, positioning the $BaO_2/Mn_2O_3/ZnO/BaMnO_3$ nanocomposite as a promising candidate for applications involving solar energy conversion, photocatalytic degradation, and photoelectrochemical processes. The ability to harness photons across a wider spectral range enhances the

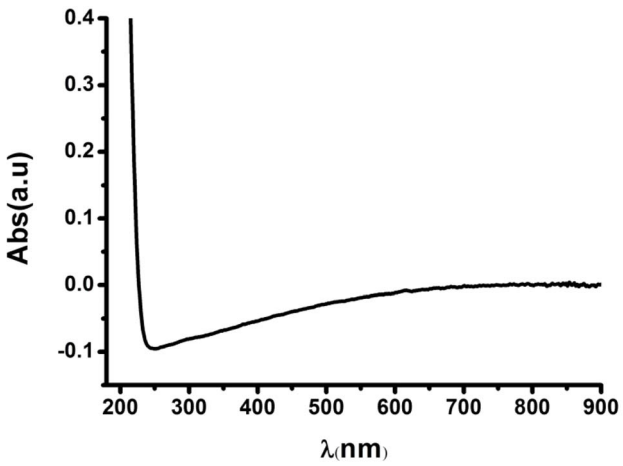

Fig. 8 The absorption spectrum of $BaO_2/Mn_2O_3/ZnO/BaMnO_3$ nanocomposite.

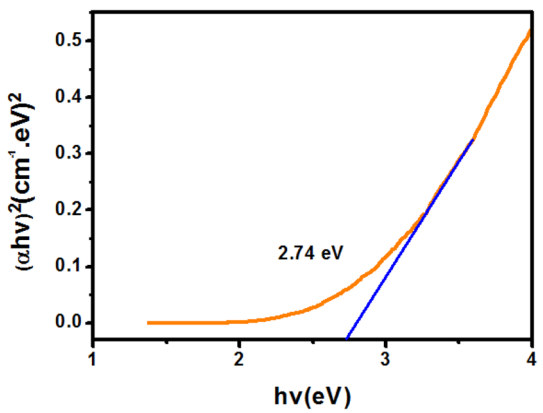

Fig. 9 The bandgap of $BaO_2/Mn_2O_3/ZnO/BaMnO_3$ nanocomposite.

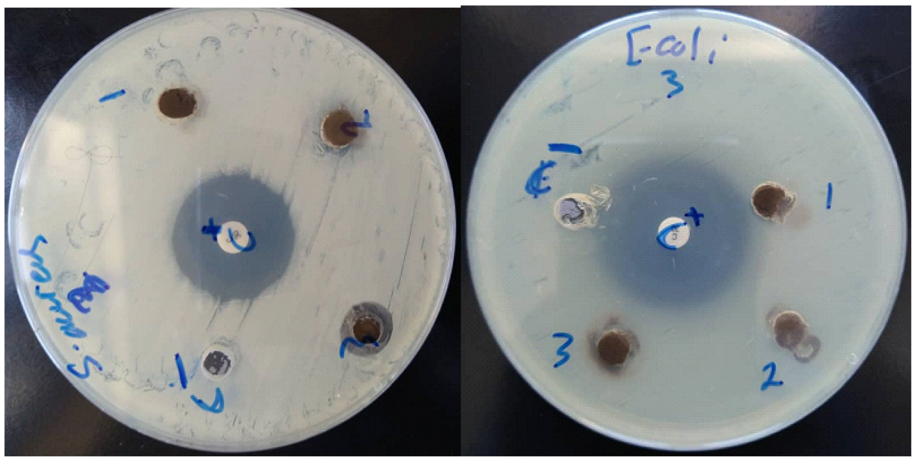

Fig. 10 Antibacterial activity of $BaO_2/Mn_2O_3/ZnO/BaMnO_3$ nanocomposite against *E. coli* and *S. aureus*. (1) 50 mg mL^{-1}, (2) 100 mg mL^{-1}, (3) 200 mg mL^{-1}, (C^+) AzM (positive control) and (C^-) (d.H_2O) (negative control).

photocatalytic efficiency and broadens potential technological applications. Furthermore, the optical properties and band structure of the nanocomposite can be systematically tuned by varying the molar ratios and synthesis parameters of the constituent oxides. This tunability offers significant scope for optimizing the nanocomposite for specific functional applications such as photovoltaic devices, water splitting, and environmental remediation. In summary, the observed band gap reduction compared to individual oxides reflects the synergistic interaction among the BaO_2, Mn_2O_3, ZnO, and $BaMnO_3$ phases in the nanocomposite, which enhances its capacity to absorb and interact with UV and visible light, confirming its suitability for diverse energy-related applications.

3.7 Antibacterial activity

The antibacterial activity of the $BaO_2/Mn_2O_3/ZnO/BaMnO_3$ nanocomposite was systematically evaluated using the disc diffusion method against two distinct bacterial strains: *Staphylococcus aureus* (*S. aureus*) (Gram-positive) and *Escherichia coli* (*E. coli*) (Gram-negative).[44,46] The assessment was conducted at varying concentrations of 50, 100, and 200 mg mL^{-1}, with the zones of inhibition measured to determine the effectiveness of the nanocomposite. The results, as illustrated in Fig. 10 and summarized in Table 4, revealed that the nanocomposite exhibited moderate antibacterial properties, particularly at concentrations of 100 and 200 mg mL^{-1}. Notably, a more pronounced antibacterial effect was observed against *S. aureus* compared to *E. coli*. This differential effectiveness can be attributed to the inherent structural differences between Gram-positive and Gram-negative bacteria. The thicker peptidoglycan layer in *S. aureus* provides a distinct target for the nanocomposite's action, while the outer membrane of *E. coli* acts as a barrier, limiting the penetration of active agents.[44,47] Furthermore, the electrostatic interactions between the positively charged metal ions (Mn^{2+}, Zn^{2+}, and Ba^{2+}) and the negatively charged surface of bacterial cells enhance the affinity of the nanocomposite for *S. aureus*, leading to greater antibacterial efficacy.[42,48]

The underlying mechanism for the observed antibacterial activity is multifaceted. The synergistic interactions among the metal ions, the unique nanostructure configuration, and the generation of reactive oxygen species (ROS) collectively contribute to its bactericidal effects agents.[49,50] The high concentration of metal ions disrupts bacterial cell membranes, ultimately inducing cell lysis and death. Additionally, the generation of ROS induces oxidative stress within bacterial cells, which is particularly detrimental to Gram-positive bacteria like *S. aureus* due to their less robust defense mechanisms against oxidative damage. Given these findings, it is evident that the $BaO_2/Mn_2O_3/ZnO/BaMnO_3$ nanocomposite holds significant promise as an effective antibacterial agent. The dual role of the nanoparticles as carriers of active metal ions and catalysts for ROS generation enhances their potential utility in antimicrobial applications. This study suggests that the nanocomposite could serve as a promising candidate for antimicrobial coatings in healthcare environments, where effective infection control measures are critical.

In conclusion, this research underscores the potential of the nanocomposite as a viable antimicrobial agent. The elucidation

Table 4 Antibacterial properties of $BaO_2/Mn_2O_3/ZnO/BaMnO_3$ at different concentrations

Name of micro organism	ZOI (mm) at various concentrations			
	50 mg mL^{-1}	100 mg mL^{-1}	200 mg mL^{-1}	Azithromycin(AzM) (control)
S. aureus	0	10 ± 0.75	13 ± 0.50	25 ± 0.75
E. coli	0	0	10 ± 0.50	30 ± 0.25

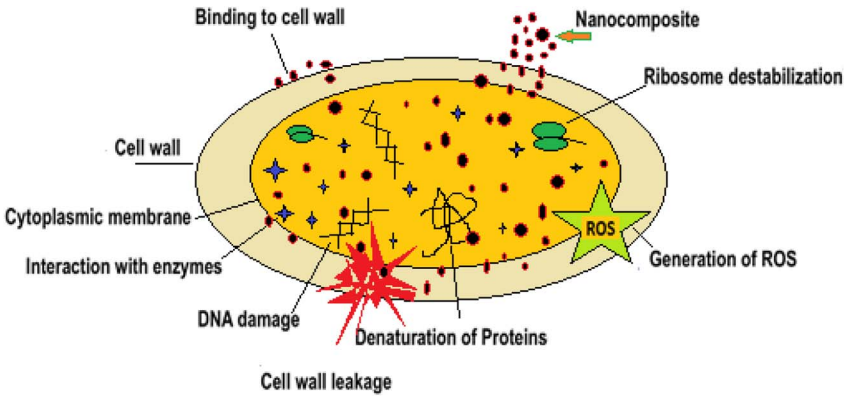

Fig. 11 Mechanism of antibacterial action in $BaO_2/Mn_2O_3/ZnO/BaMnO_3$ nanocomposite.

of its mechanism of action not only enhances our understanding of its antibacterial properties but also paves the way for the development of innovative antimicrobial therapies tailored for diverse applications in healthcare settings. Fig. 11 illustrates the proposed antibacterial mechanism of the nanocomposite, reinforcing its role as a potent agent against pathogenic bacteria.

4 Conclusion

In conclusion, this study successfully demonstrates a facile and environmentally benign synthesis route for the $BaO_2/Mn_2O_3/ZnO/BaMnO_3$ nanocomposite using distilled water as the sole solvent. Thorough structural and compositional analyses confirmed the formation of a well-defined, impurity-free nanocomposite with nanoscale crystallite dimensions. The material exhibited excellent thermal stability and a favorable optical band gap, enhancing its suitability for advanced functional applications. Moreover, its significant antibacterial activity against both Gram-positive and Gram-negative bacteria highlights its promise for antimicrobial and sterilization purposes. These findings collectively establish the nanocomposite as a versatile candidate for future development in industrial and biomedical fields. Further investigations into the underlying antibacterial mechanisms and application-specific performance are warranted to fully harness its potential.

Author contributions

Conceptualization: Adnan Alnehia and Abduelwhab B. Methodology: Adnan Alnehia and Abduelwhab B. Investigation: Mohamed E. El Sayed, Mohammad N. Murshed, and Ahmed Samir. Formal analysis: Abduelwhab B. Alwany, Adnan Alnehia and Mohammad N. Murshed. Writing – original draft: Adnan Alnehia, and Abduelwhab B. Alwany. Writing – review and editing: Mohamed E. El Sayed, Mohammad N. Murshed, and Ahmed Samir.

Conflicts of interest

The authors declare no conflicts of interest.

Data availability

The data used to support the findings of this study are included within the article.

Acknowledgements

The authors are thankful to Dr Murad Al-Asbhi for his help to perform the biological applications in Al-Hikma university laboratories, Yemen. Also, The authors extend their appreciation to the Deanship of Research and Graduate Studies at King Khalid University for funding this work through Large Research Project under grant number RGP2/359/46.

References

1 N. Pradhan, S. Singh, N. Ojha, A. Shrivastava, A. Barla, V. Rai, *et al.*, Facets of Nanotechnology as Seen in Food Processing, Packaging, and Preservation Industry, *BioMed Res. Int.*, 2015, **2015**, 17.
2 B. Mekuye and B. Abera, Nanomaterials: An overview of synthesis, classification,characterization, and applications, *Nano Select*, 2023, **4**, 486–501.
3 X. Fang, T. Zhai, U. K. Gautam, L. Wu, Y. Bando, D. Golberg, *et al.*, ZnS nanostructures: From synthesis to applications, *Prog. Mater. Sci.*, 2011, **56**, 175–287.
4 S. A. David and C. Vedhi, Synthesis and Characterization of Co_3O_4-CuO- ZrO_2 Ternary Nanoparticles, *Int. J. ChemTech Res.*, 2017, **10**, 905–912.
5 K. P. Boroujeni, Z. Tohidiyan, and H. Shahsanaei, Synthesis and characterization of Fe_2O_3/CuO nanocomposite as a new photocatalyst for solar degradation of methylene blue dye in aqueous solution, in *The 27th Iranian Conference on Organic Chemistry*, Iran, 2019.
6 A. O. Juma, E. A. A. Arbab, C. M. Muiva, L. M. Lepodise and G. T. Mola, Synthesis and characterization of CuO-NiO-ZnO mixed metal oxide nanocomposite, *J. Alloys Compd.*, 2017, **723**, 866–872.
7 A. M. Amanulla, S. K. J. Shahina, R. Sundaram, C. M. Magdalane, K. Kaviyarasu and M. Maaza, Antibacterial, magnetic, optical and humidity sensor

studies of b-CoMoO4-Co3O4 nanocomposites and its green synthesis and characterization, *J. Photochem. Photobiol., B*, 2018, **183**, 233–241.

8 M. A. Subhan, N. Uddin, P. Sarker, H. Nakata and R. Makioka, Synthesis,characterization,low temperature solid state PL and photocatalytic activities of Ag_2O, CeO.ZnO nanocomposite, *Spectrochim. Acta, Part A Mol. Biomol. Spectrosc.*, 2015, **151**, 56–63.

9 S. H. Aldirham, A. Helal, M. Shkir, M. Hadi and A. M. Ali, Synthesis of $Ag@WO_3/TiO_2$nanocomposites and their structural, optical, dielectric,electrical, and photocatalytic potentials, *Inorg. Chem. Commun.*, 2025, **179**, 114744.

10 L. Hughes, A. Roy, C. Downing, M. P. Browne, A. Zhussupbekova, I. V. Shvets, *et al.*, Surface Reduced Manganese States as a Source of Oxygen Reduction Activity in $BaMnO_3$, *Adv. Funct. Mater.*, 2023, **33**, 2214883.

11 R. Gomes, S. Roming, A. Przybilla, M. A. R. Meier and C. Feldmann, Barium peroxide nanoparticles: synthesis,characterization and their use for actuating the luminol chemiluminescence, *J. Mater. Chem. C*, 2014, **2**, 1513.

12 K. Lysien, K. Szatan, K. Szydlo, M. Polis, M. Procek, A. Stolarczyk, *et al.*, Pyrotechnic Delay Compositions Based on BaO_2 : Not as"Green" as Expected, *Molecules*, 2023, **28**, 6143.

13 N. Sharma, S. Jandaik, S. Kumar, M. Chitkara and I. S. Sandhu, Synthesis, characterisation and antimicrobial activity of manganese- and iron-doped zinc oxide nanoparticles, *J. Exp. Nanosci.*, 2016, **11**, 54–71.

14 S. Dhital, S. P. Amatya, S. Aryal, P. Neupane, N. Parajuli, MelinaTamang, *et al.*, Synthesis of Manganese Oxide Nanoparticles Using Co-Precipitation Method and Its Antimicrobial Activity, *Int. J. New Chem.*, 2024, **11**, 243–253.

15 C. J. Jafta, F. Nkosi, L. l. Roux, M. K. Mathe, M. Kebede, K. Makgopa, *et al.*, Manganese oxide/graphene oxide composites for high-energy aqueous asymmetric electrochemical capacitors, *Electrochim. Acta*, 2013, **110**, 228–233.

16 Y.-H. Son, P. T. M. Bui, H.-R. Lee, M. S. Akhtar, D. K. Shah and O.-B. Yang, A Rapid Synthesis of Mesoporous Mn_2O_3 Nanoparticles for Supercapacitor Applications, *Coatings*, 2019, **9**, 631.

17 T. S. Aldeen, H. E. A. Mohamed and M. Maaza, ZnO nanoparticles prepared *via* a green synthesis approach: Physical properties, photocatalytic and antibacterial activity, *J. Phys. Chem. Solids*, 2022, **160**, 110313.

18 A.-B. Al-Odayni, W. S. Saeed and N. A. Y. Abdu, Phyto-mediated synthesis of ZnO NPs using guava leaf extract: characterization, antibacterial activity, and hemolysis efect, *Biomass Convers. Biorefinery*, 2023, DOI: 10.1007/s13399-023-04683-y.

19 L. R., R. T., G. K. M., S. K. K., B. N. and S. B. M., Green-Synthesized Sm^{3+}-Doped ZnO Nanoparticles for Multifunctional Applications, *Adv. Mater. Sci. Eng.*, 2024, **2024**, 11, DOI: 10.1155/2024/3618390.

20 L. Hughes, A. Roy, N. Yadav, C. Downing, M. P. Browne, J. K. Vij, *et al.*, Dielectric Engineering of Perovskite $BaMnO_3$ for the Rapid Heterogeneous Nucleation of Pt Nanoparticles for Catalytic Applications, *Adv. Funct. Mater.*, 2024, **34**, 2402103.

21 A. Alnehia, H. Alnahari and A. Al-Sharabi, Characterization and antibacterial activity of $MgO/CuO/Cu_2MgO_3$ nanocomposite synthesized by sol-gel technique, *Results Chem.*, 2024, **8**, 101620.

22 A.-B. Al-Odayni, A. Naaser and Y. Abduh, synthesis of magnesium-doped copper oxide nanocomposites using tangerine peel extract: structural, optical, and bioactivity studies, *Biomass Convers. Biorefin.*, 2024, DOI: 10.1007/s13399-024-05492-7.

23 M. Hadi, Co_3O_4-CuO-ZrO_2 nanocomposite: Optical, spectral, morphological,structural and antibacterial studies, *Results Chem.*, 2024, **7**, 101311.

24 I. Kir, H. A. Mohammed, S. E. Laouini, M. Souhaila, G. H. Gamil, A. A. A. Johar, *et al.*, Plant Extract-Mediated Synthesis of CuO Nanoparticles from Lemon Peel Extract and Their Modiication with Polyethylene Glycol for Enhancing Photocatalytic and Antioxidant Activities, *J. Polym. Environ.*, 2024, **32**, 718–734.

25 M. R. Ansari, P. Agrohi and Y. Arya, Doping Effect of Alkali Earth Metal on Structural, Morphological, Optical and Magnetic Properties of Green Synthesized ZnFe2O4 Nano-particles, *Nex. Res.*, 2025, **2**, 100175.

26 D. Saravanakkumar, S. Sivaranjani, K. Kaviyarasu, A. Ayeshamariam, B. Ravikumar, S. Pandiarajan, *et al.*, Synthesis and characterization of ZnO–CuO nanocomposites powder by modified perfume spray pyrolysis method and its antimicrobial investigation, *J. Semiconduct.*, 2018, **39**, 1–7.

27 S. Saleem, A. Khalid, Z. M. Aldhafeeri, T. Alomayri, A. Ali, A. Jabbar, *et al.*, A comparative analysis of optical and electrical properties of pure CuO and Zn doped CuO nanoparticles for optoelectronic device applications, *J. Sol-Gel Sci. Technol.*, 2025, **113**, 213–224.

28 S. Saleem, M. H. Jameel, A. A. Alothman, M. Z. H. B. Mayzan, T. Yousaf, M. R. Ahmad, *et al.*, A band gap engineering for the modification in electrical properties of $Fe_3O_4$by Cu^{2+}doping for electronic and optoelectronic devices applications, *J. Sol. Gel Sci. Technol.*, 2024, **109**, 471–482.

29 A. Alnehia, A. Al-Sharabi, M. Hadi and M. A. Ahlam, Preparation and analysis of structural,morphological and optical properties of $BaFeO_{2.67}/Fe_2O_3$ nanocomposite, *Sci. Rep.*, 2025, **15**, 21822.

30 N. Abbas, J. M. Zhang, S. Nazir, H. Akhtar, M. Zaqa, S. Saleem, *et al.*, Synthesis and characterization of Fe-substituting BaO nanoparticles by sol-gel method, *Dig. J. Nanomater. Biostruct.*, 2023, **18**, 1327–1338.

31 C. Salmi, S. E. Laouini, S. Meneceur and H. A. Mohammed, Biosynthesized $MgO@SnO_2$ nanocomposite and their modiication with polyvinylpyrrolidone. Eiciency for removal of heavy metals and contaminants from industrial petroleum wastewater, *Clean Technol. Environ. Policy*, 2024, **26**, 2483–2502.

32 M. R. Ansari, S. Khaladkar, A. Kalekar, P. Pathi and K. R. Peta, Effect of annealing temperature on structural

and optical properties of $BaFe_2O_4$ nanocrystals: Energy storage applications, *J. Energy Storage*, 2025, **113**, 115650.

33 P. Djomgoue and D. Njopwouo, FT-IR spectroscopy applied for surface clays characterization, *J. Surf. Eng. Mater. Adv. Technol.*, 2013, **3**, 275–282.

34 M. S. C. Barreto, E. J. Elzinga and L. R. F. Alleoni, The molecular insights into protein adsorption on hematite surface disclosed by in-situ ATR-FTIR/2D-COS study, *Sci. Rep.*, 2020, **10**, 13441.

35 S. W. Lu, B. I. Lee and L. A. Mann, Carbonation of barium titanate powders studied by FT-IR technique, *Mater. Lett.*, 2000, **43**, 102–105.

36 A. Jayachandran, T. Aswathy and A. Nair, Green synthesis and characterization of zinc oxide nanoparticles using Cayratia pedata leaf extract, *Biochem. Biophys. Rep.*, 2021, **26**, 100995.

37 X. Huang, H. Lin and Z. Cheng, Infrared properties of perovskite manganites La1− xCa$x$$MnO_3$ with $0.25 \leq x \leq 0.45$, *Phys. B*, 2018, **529**, 16–20.

38 V. Srivastava, D. Gusain and Y. C. Sharma, Synthesis, characterization and application of zinc oxide nanoparticles(n-ZnO), *Ceram. Int.*, 2013, **39**, 9803–9808.

39 F. Kunc, M. Gallerneault, O. Kodra, A. Brinkmann, G. P. Lopinski and L. J. Johnston, Surface chemistry of metal oxide nanoparticles: NMR and TGA quantification, *Anal. Bioanal. Chem.*, 2022, **414**, 4409–4425.

40 J. Jorda and T. Jondo, Barium oxides: equilibrium and decomposition of BaO2, *J. Alloys Compd.*, 2001, **327**, 167–177.

41 S. Legmairi, S. Meneceur, G. G. Hasan, L. S. Eddine, H. A. Mohammed, F. Alharthi, *et al.*, Enhanced photocatalytic activity and antiviral evaluation of CuO@Fe_2O_3NC for amoxicillin degradation and SARS-CoV-2 treatment, *Nanotechnology*, 2023, **34**, 445101.

42 K. Karthik, S. Dhanuskodi, C. Gobinath and S. Sivaramakrishnan, Microwave-assisted synthesis of CdO–ZnO nanocomposite and its antibacterial activity against human pathogens, *Spectrochim. Acta, Part A*, 2015, **139**, 7–12.

43 V. Bhalla, C. Prabha Sahu, A. R. Shashikala, S. Singh, I. Thangavelu, S. Tadepalli, *et al.*, Synthesis and Multifunctional Evaluation of BaO_2-Sodium AlginateCurcumin Nanocomposite: Improved Antibacterial, Antioxidant, and Osteosarcoma Cell Inhibition, *J. Inorg. Organomet. Polym. Mater.*, 2025, DOI: 10.1007/s10904-025-03916-z.

44 M. M. Khan, M. H. Harunsani, A. L. Tan, M. Hojamberdiev, Y. A. Poi and N. Ahmad, Antibacterial Studies of ZnO and Cu-Doped ZnO Nanoparticles Synthesized Using Aqueous Leaf Extractof Stachytarpheta jamaicensis, *BioNanoScience*, 2020, **10**, 1037–1048.

45 S. Sharma, P. Chauhan and S. Husain, Structural and optical properties of Mn_2O_3 nanoparticles & its gas sensing applications, *Adv. Mater. Proc.*, 2016, **1**, 220–225.

46 F. Mukhtar, T. Munawar, M. S. Nadeem, M. N. u. Rehman, M. Riaz and F. Iqbal, Dual S-scheme heterojunction ZnO–V_2O_5–WO_3nanocomposite with enhanced photocatalytic and antimicrobial activity, *Mater. Chem. Phys.*, 2021, **263**, 124372.

47 A. Rahman, M. H. Harunsani, A. L. Tan, N. Ahmad, M. Hojamberdiev and M. M. Khan, Effect of Mg doping ZnO fabricated using aqueous leaf extract of Ziziphus mauritiana Lam. for antioxidant and antibacterial studies, *Bioprocess Biosyst. Eng.*, 2021, **44**, 875–889.

48 S. Nachimuthu, C. Thangamani, N. Thiyagarajulu, K. Thangaraj, D. Paramasivam, S. Thangavel, *et al.*, Facile synthesis of ZnO-Y_2O_3 nanocomposite for photocatalytic and biological applications, *Catal. Commun.*, 2023, **184**, 106786.

49 K. Kannan, D. Radhika, D. Gnanasangeetha, S. K. Lakkaboyana, K. K. Sadasivuni, K. Gurushankar, *et al.*, Photocatalytic and antimicrobial properties of microwave synthesized mixed metal oxide nanocomposite, *Inorg. Chem. Commun.*, 2021, **125**, 108429.

50 K. Kannan, D. Radhika, R. D. Kasai, D. Gnanasangeetha, G. Palani, K. Gurushankar, *et al.*, Facile fabrication of novel ceria-based nanocomposite (CYO-CSO) *via* co-precipitation: Electrochemical, photocatalytic and antibacterial performances, *J. Mol. Struct.*, 2022, **1256**, 132519.